J Mater Sci (2010) 45:168–176
DOI 10.1007/s10853-009-3912-y

Anisotropic thermal properties in orthorhombic perovskites

B. Steele · A. D. Burns · A. Chernatynskiy ·
R. W. Grimes · S. R. Phillpot

Received: 12 May 2009 / Accepted: 19 September 2009 / Published online: 6 October 2009
© Springer Science+Business Media, LLC 2009

Abstract The structure, elastic properties, thermal expansion, and thermal conductivity of the orthorhombic-structured $A^{3+}B^{3+}O_3$ perovskites are determined using atomistic simulations with classical potentials. When considered as pseudo-cubic monoclinic systems, they show relatively small deviations in structure and properties from their cubic perovskite parent phase. The variations in properties are shown to be related to the magnitude of the tilting of the BO_6 octahedra, which in turn is related to the relative sizes of the A and B ions, as encapsulated in the tolerance factor.

Introduction

The low thermal conductivity of many ceramic materials at high temperatures is critical for numerous applications, including thermal barrier coatings in gas turbines [1, 2]. While the current oxide of choice for thermal-barrier applications is yttria-stabilized zirconia (YSZ), much work is focused on the development of oxide materials with even lower thermal conductivities. Numerous other oxide materials have the potential for exhibiting lower thermal conductivity above room temperature, including the $Zr_3Y_4O_{12}$ delta phase, the tungsten bronzes, and the $La_2Mo_2O_9$ phase [3].

Due to the wide variety of crystal structures and chemistries of complex oxides, providing a physical understanding of the thermal-transport properties of these materials should prove useful in identifying strategies for the development of optimally low thermal conductivity materials. While YSZ and other fluorite-based structures such as pyrochlores are cubic and intrinsically isotropic, there are a large number of oxide-based materials that are structurally anisotropic; perovskite, ABO_3, structured materials form a particularly diverse and interesting class [4]. While the perovskite prototype structure is cubic and has the $Pm\bar{3}m$ structure, other perovskite-based structures display anisotropies of varying symmetries and degrees; moreover, there are a number of different classes of perovskite-based layered materials. In this article, we use atomic-level simulation methods to characterize the structure, elastic properties, thermal expansion, and thermal-transport properties of a series of orthorhombic (*Pbnm*) perovskites of the general form $A^{3+}B^{3+}O_3$ (3-3 perovskites) [5]. These materials are structurally quite similar to the perovskite prototype and are probably the simplest of the non-cubic perovskites. Applications of 3-3 perovskites are not limited to those requiring low thermal conductivity; for example, *Pbnm*-structured perovskites such as $LaCrO_3$ and $LaFeO_3$ have also been considered as solid oxide fuel cell cathodes [6].

Structure and symmetry of *Pbnm* perovskites

Figure 1 shows a map of the lowest-energy structure for various A–B combinations of the $A^{3+}B^{3+}O_3$ perovskite materials [5]. Here, the blue region corresponds to the hexagonal $P6_3cm$ structure, while the yellow region corresponds to the hexagonal $R\bar{3}c$ structure. The *Pbnm*-structured compounds considered here occupy the green region.

B. Steele · A. D. Burns · A. Chernatynskiy · S. R. Phillpot (✉)
Department of Materials Science and Engineering, University of Florida, Gainesville, FL 32611, USA
e-mail: sphil@mse.ufl.edu

R. W. Grimes
Department of Materials, Imperial College London,
London SW7 2AZ, UK

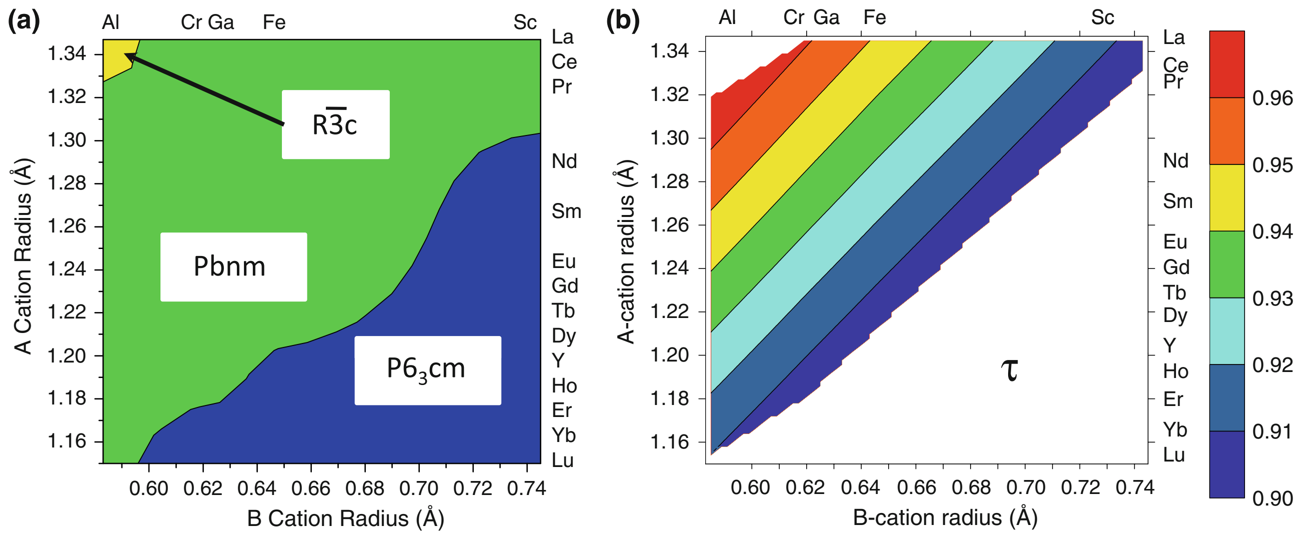

Fig. 1 **a** Stability map for the $A^{3+}B^{3+}O_3$ perovskites showing the regions in which the most stable structures are *P6₃cm*, *Pbnm*, and *R*$\bar{3}$*c* structures. **b** Map of the tolerance factor for the *Pbnm* perovskites

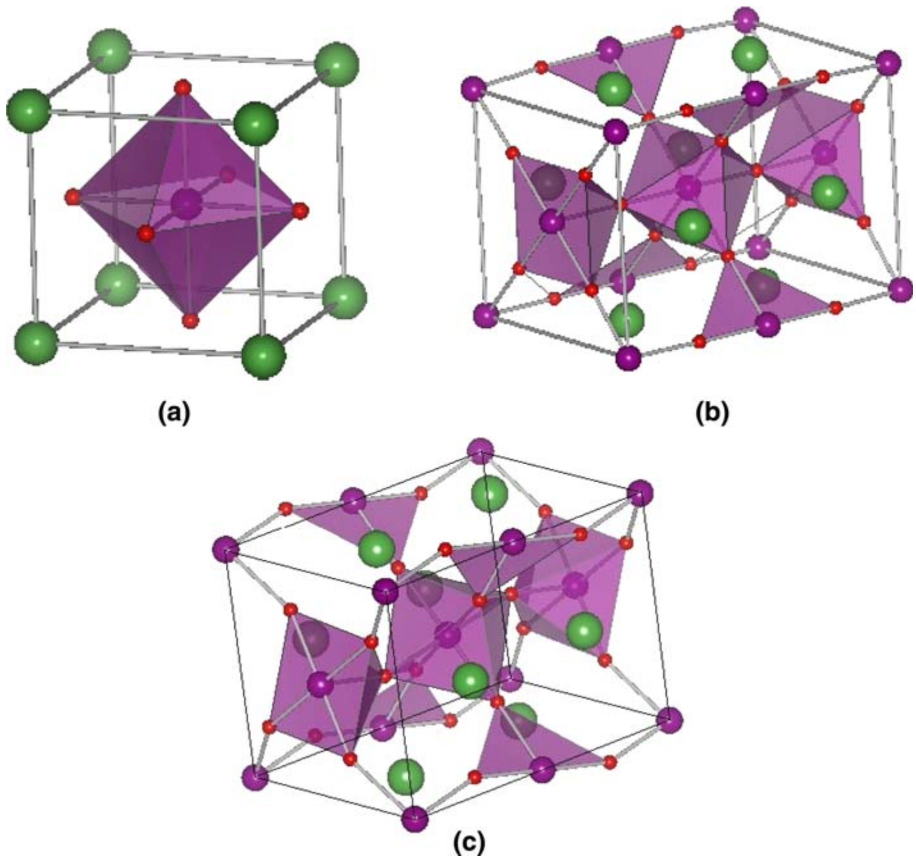

Fig. 2 **a** *Pm*$\bar{3}$*m* perovskite unit cell in the conventional ⟨100⟩ orientation containing a single stoichiometric unit of five atoms; **b** when rotated by 45° to the [1−10], [110], [001] orientation, the *Pm*$\bar{3}$*m* unit cell contains 20 atoms and; **c** *Pbnm* unit cell also containing a total of 20 atoms. Oxygens form an octahedral network, B-cations are inside of the octahedra and A-cations are atoms outside of the octahedra

It is useful to relate the *Pbnm* structure to the cubic prototype. In the perfect cubic perovskite structure, space group *Pm*$\bar{3}$*m*, Fig. 2a, the oxygen atoms form an octahedron around the B atom. These octahedra are connected at their vertices, such that the diagonals of each octahedron are parallel to the corresponding diagonals of all of the neighboring octahedra.

The two cations are generally not of the ideal size to fit inside their polyhedra. The size discrepancy can be characterized by the tolerance factor, τ:

$$\tau = \frac{R_A + R_O}{\sqrt{2}(R_B + R_O)}$$

where R_A, R_B, and R_O are the ionic radii of the A cation, B cation, and oxygen ion, respectively; here, the Shannon radii [7] appropriate to the specific coordination (twelve-fold for A, six-fold for B) are used. From this equation, it can be seen that τ decreases as the R_B/R_A ratio increases, as shown in Fig. 1b. For $\tau = 1$, the relative ionic radii of A and B are be such that they fit into the cubic perovskite lattice without any strain; the structure would then be expected to be that of the cubic prototype. (This analysis does not take into account the additional complexities arising from ferroelectric and antiferrodistortive instabilities present in many 2-4 and 1-5 perovskites.) We expect deviations from the cubic structure to increase the more τ deviates from unity; thus, we anticipate larger deviations from the cubic structure the more we go from the top left to the bottom right of the tolerance-factor map in Fig. 1b.

To provide a reference against which to compare the *Pbnm* structure, it is useful to consider the $Pm\bar{3}m$ structure in an orientation rotated by 45° around $\langle 001 \rangle$, as shown in Fig. 2b. In this orientation, the edges of this larger unit cell are aligned with the [1−10], [110], and [001] directions of the ideal cubic perovskite unit cell. This rotated unit cell is tetragonal, with the *a* and *b* lattice parameters having the length of the surface diagonals in the ideal cubic unit cell. If the lattice parameter of the cubic perovskite is taken to be a_0, then the lattice parameters in this rotated coordinate system are $a{:}b{:}c = \sqrt{2}a_0{:}\sqrt{2}a_0{:}2a_0$; that is, they are in a $1{:}1{:}\sqrt{2}$ ratio.

The *Pbnm* perovskite structure can be viewed as a [110]-oriented perovskite structure, Fig. 2b, whose symmetry is broken by the octahedra being tilted. Figure 2c shows the *Pbnm* unit cell in which the octahedra are tilted with respect to their neighbors in a specific repeating pattern, as described below, giving rise to an orthorhombic unit cell.

It should be noted that there is no unique choice as to which crystallographic direction is taken as the long direction of the orthorhombic unit cell. The above analysis took the *c*-direction as the long direction. If, however, the *b*-direction had been taken as the long direction, then the structure would be described as *Pnma* rather than *Pbnm*, while if the *a*-direction had been taken as the long direction, as in Glazer's [8] article analyzing tilting behavior in perovskites, the structure would be described as *Pmnb*. These three symmetry descriptions are thus all manifestations of Space Group No. 62 [9].

In his analysis of tilting behavior [8], Glazer started with a 2 × 2 × 2 (001)-oriented perfect perovskite supercell, and then characterized the cell parameters as a result of all different possible tilting schemes. The pattern of tilting for *Pbnm* materials is $a^+b^-b^-$. In this notation, "*a*" and "*b*" refer to the relative magnitudes of the tilt angles around the supercell lattice axes. The "+" and "–" refer to different relative tilt orientations between parallel planes of octahedra. The "+" means successive parallel planes are tilted in the same direction, as illustrated in Fig. 3a, b, while the "–" means the parallel planes alternate in tilting directions, as illustrated in Fig. 3c, d. As an alternative to the *Pbnm* unit cell, one can analyze these systems in Glazer's non-orthogonal pseudo-cubic unit cell, derived from a 2 × 2 × 2 (001)-oriented perfect perovskite cell. That cell has $a = b \neq c$ (note, that we choose the *c*-direction to be different from the *a*- and *b*-direction, a different choice than that of Glazer), with the angle between *a* and *b* deviating from 90°. In this pseudo-cubic cell, the system can be analyzed as a monoclinic system; of course, it actually has additional symmetries that render it orthorhombic, including the fact that *a* is equal to *b*.

While it is convenient to perform all the calculations and simulations in the orthogonal *Pbnm* unit cell, it is more illuminating to report all the results using this pseudo-cubic cell, since it more closely reflects the symmetries of the parent $Pm\bar{3}m$ perovskite cell, with small deviations caused by the tilting.

Since we will analyze the thermal and elastic properties of these materials, it is important to understand their symmetries. Thermal expansion is a second-rank tensor. For the $Pm\bar{3}m$ structure, the thermal expansion coefficient is the same in all three directions in both the [100]- and [110]-oriented unit cells, and the thermal-expansion tensor collapses to a single scalar coefficient. For the orthorhombic structure, the thermal-expansion coefficient tensor is diagonal and can be characterized by α_a, α_b, and α_c. In the monoclinic system, off-diagonal elements between the *x*- and *y*-direction appear. Carrying out the transformation of the coordinate system, the pseudo-cubic monoclinic thermal expansion α_M, in terms of the orthorhombic thermal expansion tensor is given by:

$$\alpha_M = \begin{pmatrix} \frac{1}{2}(\alpha_a + \alpha_b) & \frac{1}{2}(\alpha_a - \alpha_b) & 0 \\ \frac{1}{2}(\alpha_a - \alpha_b) & \frac{1}{2}(\alpha_a + \alpha_b) & 0 \\ 0 & 0 & \alpha_c \end{pmatrix}.$$

Although the symmetry is different, the thermal expansion tensor in the pseudo-cubic monoclinic reference frame has three distinct components as it did in the orthorhombic reference frame. The symmetry properties of the thermal conductivity are identical to that of the thermal expansion, since it is also a second-rank tensor.

The elastic constant tensor for the cubic $Pm\bar{3}m$ perovskite unit cell has only three distinct elastic constants, C^c_{11}, C^c_{11} and C^c_{44}. The *Pbnm* structure reduces the symmetry to that of an orthorhombic system with nine distinct elastic constants: C^O_{11}, C^O_{22}, C^O_{33}, C^O_{12}, C^O_{13}, C^O_{23}, C^O_{44}, C^O_{55} and C^O_{66}. The 20-atom unit cell shown in Fig. 2b is tetragonal and is

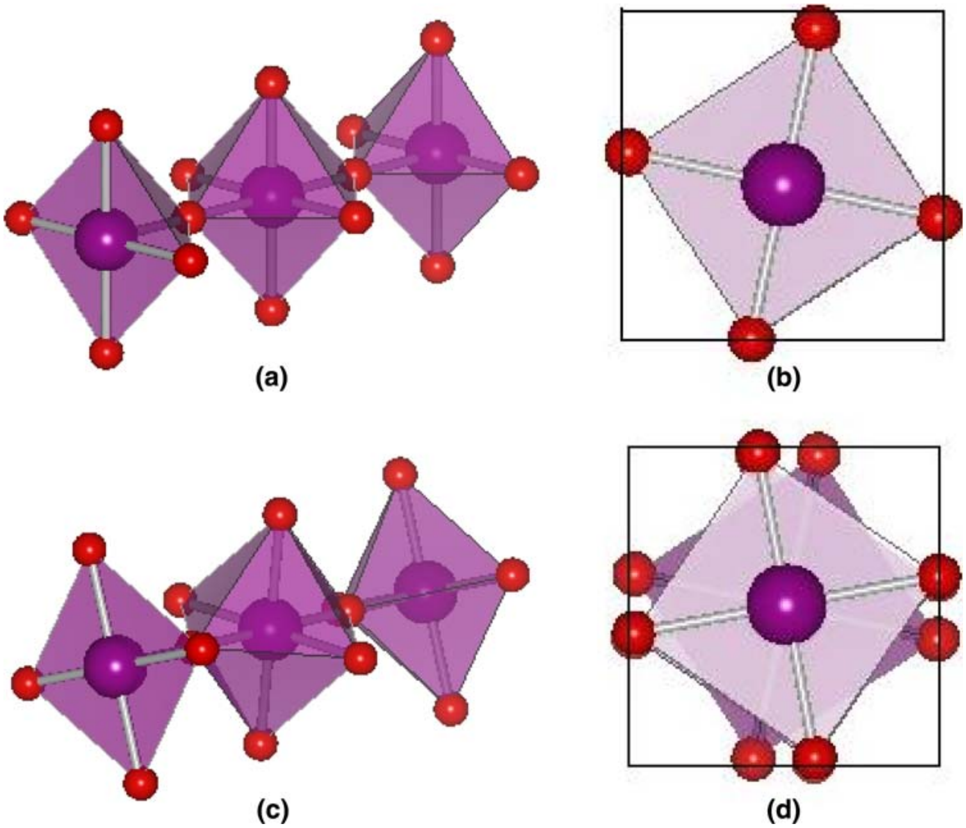

Fig. 3 Schematic showing octahedra with the "+" tilt orientation from **a** angled view, **b** axial view against cubic cell reference; and with the "−" tilt orientation from **c** angled view, **d** axial view against cubic cell reference

thus described by the elastic constants: $C^t_{11} = C^t_{12}$, C^t_{33}, C^t_{12}, $C^t_{13} = C^t_{23}$, C^t_{44} and $C^t_{55} = C^t_{66}$. The elastic constants in the tetragonal unit cell are related to those in the cubic unit cell by the usual rotational transformations [10]. The pseudo-cubic monoclinic system has 13 non-zero elastic constants (since this is the same physical structure as orthorhombic cell, only 9 of them are independent): $C^m_{11} = C^m_{22}$, C^m_{33}, C^m_{12}, $C^m_{13} = C^m_{23}$, $C^m_{16} = C^m_{26}$, C^m_{36}, $C^m_{44} = C^m_{55}$, C^m_{45}, and C^m_{66}. Equalities between some of these constants are again due to the fact that a is equal to b in the pseudo-cubic cell.

Simulation methods

In our simulations, the interatomic interactions operate through Coulombic interactions and through short-ranged interactions described by the Buckingham potential:

$$V(r_{ij}) = A\mathrm{e}^{-r_{ij}/\sigma} + \frac{B}{r_{ij}^6}.$$

Here, r_{ij} is the distance between ions i and j, and A, B, and σ are parameters specific to each interaction. We use the parameters previously determined by Levy et al. [5].

The structural parameters and elastic constants were determined using conventional lattice statics methods as implemented in using the General Utility Lattice Program (GULP) [11, 12]. We also used GULP to determine the thermal expansion within the quasi-harmonic approximation (QHA) to lattice dynamics. The GULP results were compared with the results of MD simulations obtained from a well-tested and verified in-house code. Figure 4 shows the results for the lattice parameter of $NdFeO_3$, a typical example. The thermal expansion coefficients (the slopes of the lattice parameters as a function of

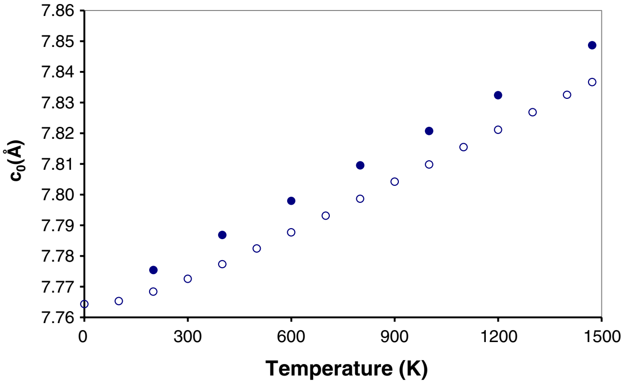

Fig. 4 Lattice parameter c of $NdFeO_3$ as a function of temperature as determined using lattice dynamics in the quasi-harmonic approximation (*open symbols*) and from MD simulations (*solid symbols*)

temperature) do not match at low temperatures because the QHA calculations include quantum effects (by using full Bose–Einstein distribution functions for the average number of phonons in a given state), while the MD simulations do not (MD simulation reproduces Maxwell–Boltzmann statistics, which differ from the correct Bose–Einstein statistics at low temperatures) [13]. However, over the temperature range of 500–1,200 K, the two methods yield similar thermal expansion coefficients: $\alpha_c^{QHA} = 7.14 \times 10^{-6}\ K^{-1}$ versus $\alpha_c^{MD} = 7.79 \times 10^{-6}\ K^{-1}$. This result underestimated the experimental value [14] of $13.3 \times 10^{-6}\ K^{-1}$. However, this seems to a rather general shortcoming of the Buckingham-type potentials, observed previously in the other oxide systems [15], as well as perovskites [16]. Corresponding levels of agreement were obtained for the other components of the thermal expansion tensor and for the other *Pnma* compositions considered here. As a result, our analysis of thermal expansion is based on the results of the QHA calculations, which are much less computationally intensive.

Conventional non-equilibrium MD methods were used to determine the thermal conductivity [17]. In brief, the system consisted of a long rectangular block oriented along the principal crystallographic directions of the *Pbnm* system. All simulations were carried out using 3-D periodic boundary conditions. The long direction of the square cylinder was successively alternated among the orthorhombic *a*-, *b*-, and *c*-axis, thereby allowing the thermal conductivity to be calculated in all three directions. As shown in the top panel of Fig. 5, heat was added and removed from equally spaced slices of the system, so as to set up two identical heat fluxes. This eventually resulted in a temperature gradient as heat flowed from the hot to cold region as shown in the lower panel of Fig. 5. The heat flux and temperature gradient were then used to calculate the thermal conductivity via Fourier's law:

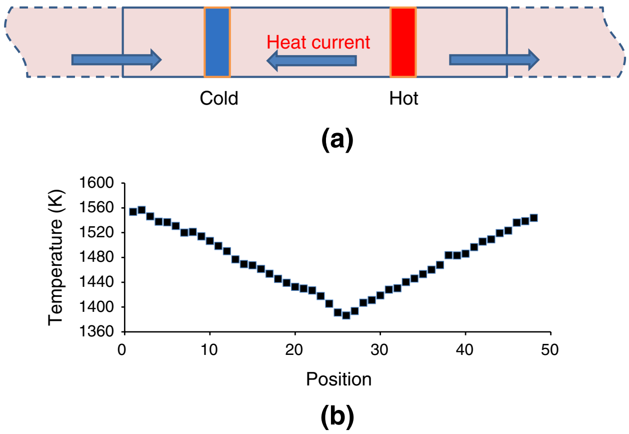

Fig. 5 (*Top*) Schematic of the thermal conductivity simulation; note that the system is periodic in all three directions. (*Bottom*) Calculated temperature profile for the case of $DyGaO_3$ in the orthorhombic *a*-direction

$$j_i = -\kappa_i \frac{dT}{dr_i},$$

where κ_i corresponds to the *a*, *b*, or *c* crystallographic directions, and j_i and dT/dr_i are the heat current and temperature gradient, respectively, in the same direction. As was discussed in detail in ref. [18], the statistical error for the thermal conductivity as calculated by non-equilibrium dynamics is typically about 10%.

Structural analysis

The deviation of the pseudo-cubic unit cell from an ideal cubic structure is conveniently characterized in the pseudo-cubic orientation by the volume *V* and the deviation of the angle between *a* and *b* from 90°, Θ_{ab}. Figure 6 shows contour plots of these quantities, as obtained from GULP, for the lattice parameters of each material.

Figure 6a shows that, as expected, the volume of the unit cell increases with increasing ionic radii of both A and B cations (i.e., from bottom left to top right). One can also observe that the B-cation has a larger influence on the volume of the unit cell. This is actually a rather general trend, manifested in a number of properties; the origin of this will be discussed below. Also, in accord with the trends expected from the tolerance factor, Fig. 1b, Θ_{ab} deviate more strongly from the ideal values as we proceed from top left to bottom right, i.e., as the tolerance factor deviates more strongly from unity.

The tilting of the octahedra is an ion-size effect. Taking the ideal $Pm\bar{3}m$ perovskite structure as the reference state, then for a fixed B radius (i.e., fixed size of the octahedra) as the A ionic radius decreases, the A–A cation distance (i.e., the lattice parameter) should decrease. The only way that this can happen without distorting the octahedra is for them to tilt. Correspondingly, if the A ion's radius is fixed and the B ion radius increases, the size of the octahedra increases. The only way to accommodate these larger octahedra is also for them to tilt. Thus, tilting increases if the B radius increases and/or the A radius decreases, i.e., when the tolerance factor decreases from unity as we go from top left to bottom right. Figure 7 shows the magnitudes of the tilting angles, α and γ around the [100] and [001] directions of the pseudo-cubic unit cell, and demonstrates that this is indeed the case. The magnitudes of these tilting angles are somewhat different from each other, with the γ angle being the larger of the two. This seems to imply that the tilting type contributes to the magnitude of the tilt: in the direction with the "−" tilt type the tilts of successive octahedra are in opposite directions, hence if

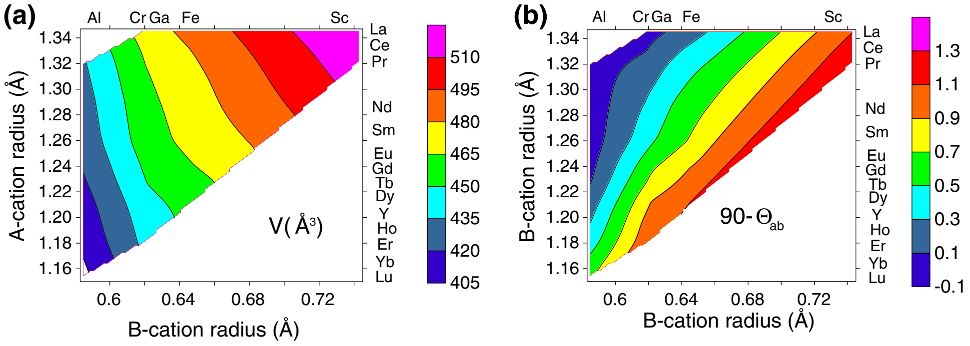

Fig. 6 Contour plots at 0 K of **a** unit cell volume and **b** deviation of the angle between *a*- and *b*-axis from 90°. The *white areas* correspond to regions in which the *Pbnm* structure is not the equilibrium structure (see Fig. 1)

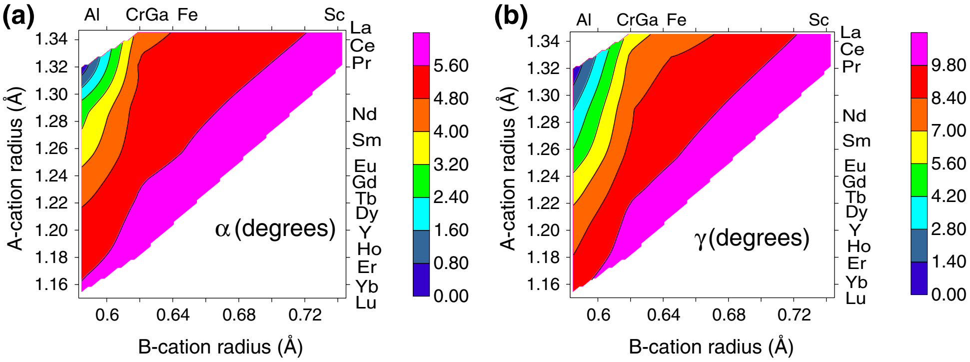

Fig. 7 Tilt angles α and γ

there are "torsion" forces in the system they would prevent large tilting. Correspondingly, in the direction of "+" tilting, successive octahedra all tilt in the same direction; therefore, the overall tilting may be larger.

Elastic properties

Figure 8 shows representative elastic constants. Figure 8a shows that C_{11} undergoes a softening of about one-third across the range of stability of the *Pbnm* phase, which is directly correlated to the increase in the *a* lattice parameter and in the unit cell volume, Fig. 6a. Just as in the case of the volume, the dependence on the B-cation size is greater than on the A-cation size. All the elastic constants that are zero in the ideal cubic structure (C_{12}, C_{13}, C_{23}, C_{22}, C_{33}, C_{44}, C_{55}, C_{66}) show a similar behavior, with the exceptions of C_{33} and C_{44}, which are completely independent of the size of the A-cation (C_{44} is shown on Fig. 8c). A typical example of an elastic constant whose value is zero in the ideal structure, C_{45}, is shown in the Fig. 8d. These non-zero values arise from the deviations from the ideal cubic symmetry, and are therefore small. The trend in C_{45} is the same as the tolerance factor: it increases from left top to the bottom right.

Over the entire map $C_{11} = C_{22}$, and C_{33} have very similar values, which is consistent with the only small departure from the ideal cubic symmetry. Likewise, C_{13} and C_{23} are very similar to each other, as are C_{44} (C_{2323}), C_{55} (C_{1313}) and C_{66}(C_{1212}).

Thermal expansion

There are many materials that display anisotropic thermal expansion. For example, alumina shows a weak anisotropy in the thermal expansion (8.3×10^{-6} K^{-1} in the *a*–*b* plane vs. 9.0×10^{-6} K^{-1} in the *c*-direction) [19]. Titania (TiO_2) shows a larger anisotropy, 4.5×10^{-6} K^{-1} versus 8.4×10^{-6} K^{-1} for anatase, and 7.00×10^{-6} K^{-1} versus 9.37×10^{-6} K^{-1} for rutile at room temperature [20]. These anisotropies arise because the structures are inherently anisotropic. The systems considered here are also structurally anisotropic. However, as we have seen the anisotropy in these systems is of a somewhat different nature because it is possible, at least in principle, to span a range from no anisotropy to high anisotropy simply by changing the A and B ions. The thermal expansion tensor for each material was calculated using GULP as described in "Structural analysis" section.

Figure 9 presents components of the thermal expansion tensor. It should be noted that in the directions in which there is a "−" tilting pattern, the thermal expansion decreases from top right to bottom left, or from weaker to stronger structural anisotropy. However, in the *c*-direction, which has a "+" tilting pattern, the trend is reversed. As

Fig. 8 Maps of elastic constant in GPa for **a** C_{11}, **b** C_{12}, **c** C_{44}, **d** C_{45} of the pseudo-cubic lattice

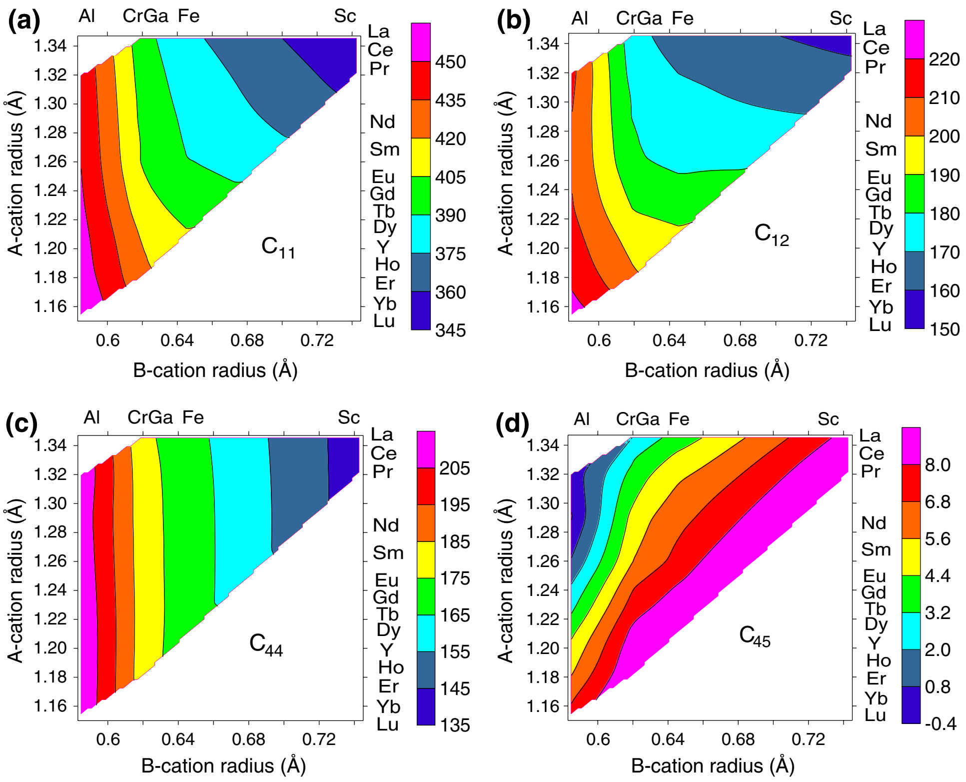

Fig. 9 Thermal expansion coefficients in units of 10^{-6} K^{-1} for **a** α_{11}, **b** α_{12}, and **c** α_{33}

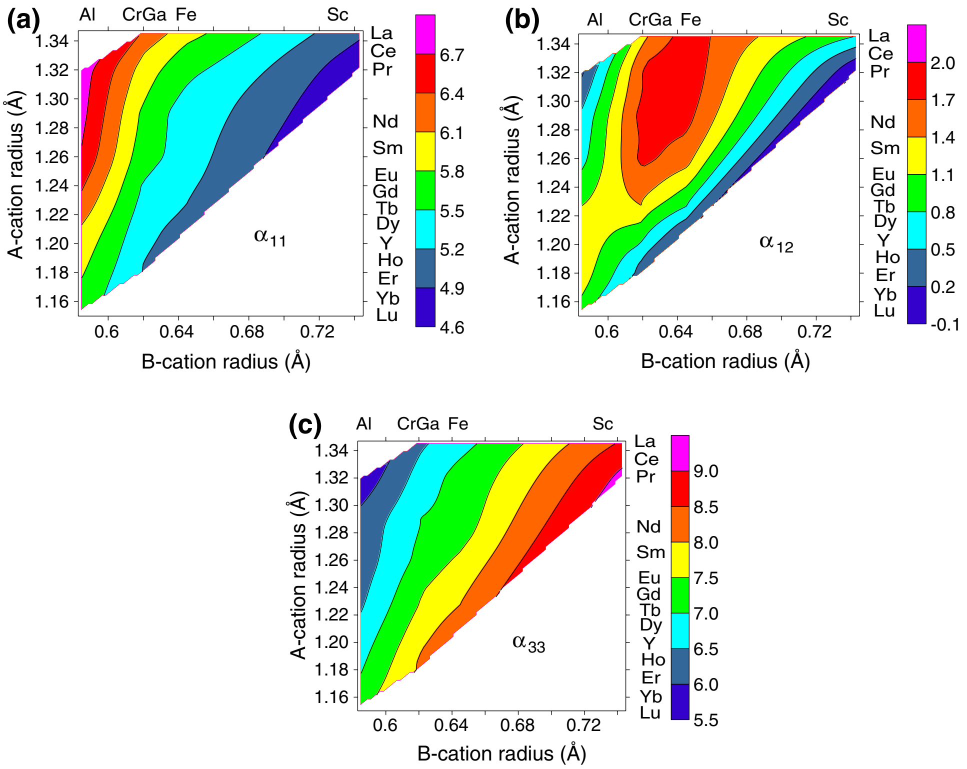

Glazer notes, any tilt around the axes in the *a*–*b* plane results in a decrease in the length of the *c*-axis. This means that a larger *a*–*b* tilt result in the atoms being pushed closer together in the *c*-direction, which further results in the atoms exerting more force on one another upon heating. This, in turn, should increase the thermal expansion in that direction (the *c*-direction) as is indeed the case.

The decrease in thermal expansion in the *a*- and *b*-direction as the tolerance factor decreases is due to the associated increase in the "−" tilting pattern in the *a–b* plane. Notice in Fig. 3d that as the tilt increases, the atoms along the upper vertices move further apart in the plane of the figure, though they may move closer together in the direction normal to the figure. This does not, however, hold true for the "+" tilting pattern shown in Fig. 3b. This could mean that greater tilt actually results in more space between atoms in the *a–b* plane, which would reduce thermal expansion in the *a*- and *b*-direction.

Recall that the off-diagonal elements of the thermal expansion tensor are zero for the cubic perovskite phase. Here, they have values that are about 30% of the values for the diagonal elements, and after an initial increase in accord with decreasing tolerance factor (as one travels from the top left to bottom right) they start to decrease again, indicating a smaller anisotropy in thermal expansion in *xy*-plane. This result is somewhat surprising, but is most likely just a reflection of the overall reduction of thermal expansion in the *xy*-plane. Just as in the case of the elastic constants, the thermal expansion depends more strongly on of the B-cation size than the A-cation size.

Thermal conductivity

Four materials have been the subject of complete thermal conductivity analysis: $NdFeO_3$, $NdAlO_3$, $GdFeO_3$, and $HoAlO_3$. These four materials were specifically chosen to allow comparison between materials where only the A or B atom varies, as well as to allow analysis of trends in thermal conductivity parallel and perpendicular to the phase boundary depicted in Fig. 1a. Additionally, these four materials represent points over a broad range of the *Pbnm* region. This method of sampling greatly reduces the number of calculations for analysis, while still yielding significant results for trend analysis.

The four materials, two with the same A site ion and two with the same B site ion strongly suggest trends in behavior. First, $k_{11} < k_{33}$ for all four systems. This again is attributable to the different tilting schemes in different directions. The "−" tilting scheme rotates subsequent octahedra in opposite direction, thus introducing a comparatively larger degree of disorder than "+" tilting, for which octahedra tilt in the same way. We would expect such increased disorder to be associated with a smaller thermal conductivity. Second, determining the precise value of k_{12} is actually quite difficult because it is calculated from the difference in the simulation values of the thermal conductivity in the orthorhombic structure (corresponding results are presented in the fourth and fifth columns of Table 1); all four system yield rather small values, as is expected for systems with only small deviations from the cubic structure. Third, the two B = Fe systems have very similar thermal conductivities; the two B = Al systems have somewhat different thermal conductivities; however they are both larger than those for B = Fe. Moreover, the two A = Nd systems have thermal conductivities that differ by more than a factor of two. Taken together, these results show that thermal conductivity depends strongly on the B ion, but only weakly on the A ions.

Table 1 Calculated thermal conductivity in units of W m^{-1} K^{-1} for four representative ABO_3 perovskites

	κ_{11}	κ_{12}	κ_a	κ_b	$\kappa_{33}(\kappa_c)$
$NdFeO_3$	2.71	0.03	2.74	2.68	3.01
$NdAlO_3$	6.17	0.45	6.61	5.72	6.59
$GdFeO_3$	2.61	0.11	2.72	2.50	2.76
$HoAlO_3$	4.27	0.26	4.53	4.01	5.16

κ_{11} and κ_{12} are the components of the thermal conductivity in the pseudo-cubic cell, while κ_a and κ_b are for the orthorhombic unit cell

We note that in addition to the structural properties, the thermal conductivity is also sensitive to the mass variations among atoms that form a structure. B-cations are lighter elements with atomic mass varying by more than a factor of two from 27.0 for Al to 69.7 for Ga. Moreover, as the mass of the B-cation increases, so does the mass mismatch between B-cation and oxygen atoms, which enclose them; this should lead to a decrease in the thermal conductivity with increasing B-atom mass. A-cations, on the other hand, are comparatively heavy elements with atomic mass ranging from 138.9 a.u. for La to 174.6 a. u. for Lu. These relatively large masses and their relatively small range of variability comparing to B-cations (only around 50%) are consistent with only a weak effect on thermal conductivity. This is in full agreement with the data presented in Table 1: heavy-Fe containing compounds have thermal conductivity only approximately half of those of light-Al-containing compounds. Changes in thermal conductivity for differing A-cations seems to be more affected by the structural changes: the thermal conductivities of $NdFeO_3$ and $NdAlO_3$ (with high tolerance factors) are higher than thermal conductivities of $GdFeO_3$ and $HoAlO_3$, respectively (with low tolerance factors).

To characterize these trends more clearly, we have determined the thermal conductivity of a series of systems in which either the A or B ion is varied, but not both. Due to the intense computational load of such simulations, these were only performed for the *a*-direction of the orthorhombic lattice. Figure 10a shows the thermal conductivity as a function of ionic radius for the $AGaO_3$ systems (from

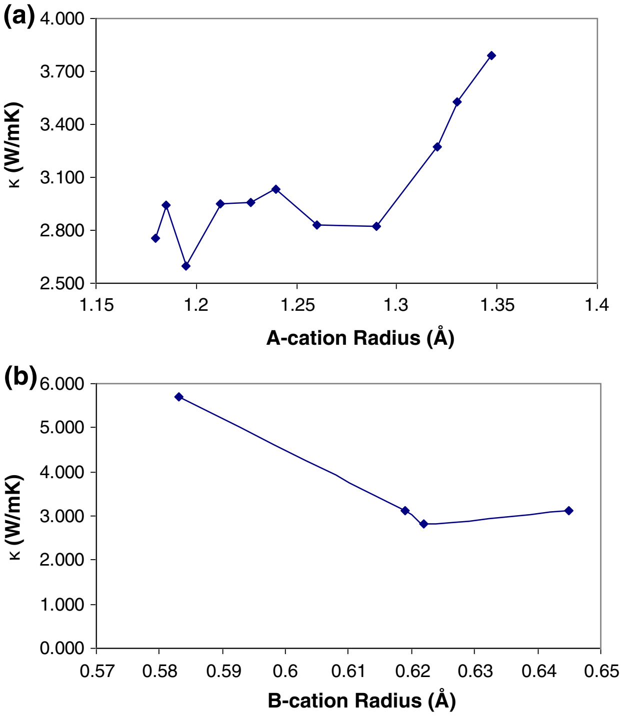

Fig. 10 Calculated thermal conductivity in units of W m^{-1} K^{-1} for **a** with $AGaO_3$ (A = Ho, Y, Dy, Tb, Gd, Eu, Sm, Nd, Pr, Ce, La) and **b** $NdBO_3$ (B = Al, Ga, Cr, Fe). All measurements are along the orthorhombic *a*-direction

left to right: A = Ho, Y, Dy, Tb, Gd, Eu, Sm, Nd, Pr, Ce, La). Comparing to Fig. 1b, the tolerance factor is increasing from left to right in Fig. 10a. Just as we would expect from the previous discussion, the thermal conductivity increases with the ionic radius, i.e., as the tolerance factor increases and the system becomes closer to being cubic. Correspondingly, the $NdBO_3$ (from left to right B = Al, Ga, Cr, Fe) systems (Fig. 10b) correspond to moving from left to right in Fig. 1b, thereby decreasing the tolerance factor and increasing in structural disorder. As discussed above, the mass effect plays a significant role in this case: Al is significantly lighter than other elements discussed and have lesser mass mismatch with oxygen.

Discussion and conclusions

In this article, we have systematically studied the effect of composition on the mechanical and thermal properties of orthorhombic-structured $A^{3+}B^{3+}O_3$ perovskites. Structural parameters, elastic constants, thermal expansion, and thermal conductivities were determined using atomistic simulations with interatomic interactions described by empirical classical potentials. All of the properties showed significantly stronger dependence on the type of B-cation than on the A-cation. A similar effect was found previously by Schelling et al. [15] for the case of the $A_2B_2O_7$ pyrochlore system and was explained by the stronger bonding of the B-cation to the oxygen, as compared with A-cation–oxygen bond. Indirect evidence for this difference in bonding strength is also provided by the DFT calculations [21] on the isostructural perovskite material, in which the B–O was found to be covalent, while all of the other bonds were ionic. Based on these arguments, we conclude that it is likely that B–O bond is stronger than A–O bond in the orthorhombic perovskites and is responsible for the observed behavior. The structural parameters (tilt angles) and thermal expansion are most significantly affected by the $a^+b^-b^-$ tilting characteristic of these materials. In particular, both the larger tilt with respect to the *c*-axis, and the opposite trends in thermal expansion along the *a*- and *c*-axis were found to be consequences of the tilting scheme. The thermal conductivity was also found to be controlled by the B-cation.

Acknowledgements We are happy to acknowledge valuable conversations with Prof. David Clarke (Harvard) and Prof. Susan Sinnott (UF). This work was supported by a Materials World Network Project, NSF DMR-0710523 and EPSRC EP/F026463/1. The work of AC was supported by DARPA.

References

1. Meier SM, Gupta DK (1994) J Eng Gas Turbines Power 116:250
2. Clarke DR, Levi CG (2003) Ann Rev Mater Res 33:383
3. Winter MR, Clarke DR (2007) J Am Ceram Soc 90:533
4. Mitchell RH (2002) Perovskites: modern and ancient. Almaz Press, Thunder Bay
5. Levy MR, Grimes RW, Sickafus KE (2004) Philos Mag 84:533
6. Jiang S, Chan S (2004) J Mater Sci 39:4405. doi: 10.1023/B:JMSC.0000034135.52164.6b
7. Shannon RD (1976) Acta Crystallogr A32:751
8. Glazer AM (1972) Acta Crystallogr B28:3384
9. International Tables for Crystallography Online (2006) Springer, New York
10. Nye JF (1985) Physical properties of crystals: their representation by tensors and matrices. Oxford University Press, Oxford
11. Gale JD, Rohl A (2003) Mol Simul 29:291
12. Gale JD (1997) J Chem Soc Faraday Trans 93:629
13. Turney JE, McGaughey AJH, Amon CH (2009) Phys Rev B 79:224305
14. Sławiński W, Przeniosło R, Sosnowska I, Brunelli M, Bieringer M (2007) Nucl Instrum Methods B 254:149
15. Schelling PK, Phillpot SR, Grimes RW (2004) Philos Mag Lett 84:127
16. Williford R, Stevenson J, Chou S, Pederson L (2001) J Solid State Chem 156:394
17. Schelling PK, Phillpot SR (2001) J Am Ceram Soc 84:2997
18. Stevens RJ, Zhigilei LV, Norris PM (2007) Int J Heat Mass Transf 50:3977
19. Yates B, Cooper RF, Pojur AF (1972) J Phys C Solid State Phys 5:1046
20. Hummer DR, Heaney PJ, Post JE (2008) Powder Diffr 23:267
21. Usvyat DE, Evarestov RA, Smirnov VP (2004) Int J Quantum Chem 100:352